

Domain-Pattern Transfer across an Artificial Magnetoelectric Interface

Gabriele De Luca,^{1,*†} Peggy Schoenherr,¹ Johannes Mendil,² Dennis Meier,³ Manfred Fiebig,¹ and Morgan Trassin¹

¹*Department of Materials, ETH Zurich, Vladimir-Prelog-Weg 4, 8093 Zurich, Switzerland*

²*Department of Materials, ETH Zurich, Hönggerbergstrasse 64, 8093 Zurich, Switzerland*

³*Department of Materials Science and Engineering, Norwegian University of Science and Technology (NTNU), Sem Sælandsvei 12, 7491 Trondheim, Norway*



(Received 31 May 2018; revised manuscript received 13 September 2018; published 13 November 2018)

Magnetoelectric interfaces provide efficient pathways for manipulating the magnetic order with low-power-consuming electric fields. A prime example of this is the voltage-controlled domain-pattern transfer from a multiferroic BiFeO_3 film into an amorphous $\text{Co}_{0.9}\text{Fe}_{0.1}$ ferromagnetic layer. Here we use a combination of optical second-harmonic generation and magnetic force microscopy to scrutinize the evolution of this transfer under voltage application. The nondestructive nature of our analysis permits the *in operando* examination of the magnetoelectric poling. We trigger ferroelectric switching events in BiFeO_3 and track the evolution of their magnetoelectric transfer to the ferromagnetic domains of $\text{Co}_{0.9}\text{Fe}_{0.1}$ with spatial resolution. This reveals a wake-up effect in the magnetoelectric coupling across the interface. It is followed by simultaneous 90° rotations of the in-plane net polarization and net magnetization that progress with the increase of the voltage applied to the device.

DOI: [10.1103/PhysRevApplied.10.054030](https://doi.org/10.1103/PhysRevApplied.10.054030)

I. INTRODUCTION

The possibility of controlling magnetization with an electric field enables the development of electronic devices with drastically reduced energy consumption [1–4]. Multiferroic materials, in which such a magnetoelectric (ME) manipulation is achieved, have experienced a resurgence of interest during the last few years [5]. The scarcity of room-temperature ME multiferroics—that is, materials with coexisting and coupled ferroelectric (FE) and ferromagnetic (FM) orders—encouraged research on composite multiferroic materials, in which a FM magnetostrictive constituent and a FE piezoelectric constituent are combined in granular or layered form [6]. More-controlled approaches implement the desired ME functionality at or across well-defined interfaces of heterostructures [7–9], for example, using piezoelectric substrates [10], or by directly tuning the magnetic anisotropy with an electric field [11,12] or, very recently, by atomically engineering the ferroic phases in an oxide superlattice [13].

The ultimate goal of a room-temperature electric-field-induced reversible switching of the magnetization was realized by the combining of multiferroic BiFeO_3 (BFO)

with $\text{Co}_{0.9}\text{Fe}_{0.1}$ (CoFe) [14–16]. In BFO, FE and antiferromagnetic (AFM) orders are bound together [17]. For a [001]-oriented BFO film, which stabilizes its ferroelectric order by formation of a stripe-domain pattern, it was shown that a canted interfacial magnetic moment, linked one-to-one to the electric dipole moment, can drive the coupling between the AFM order and the FM order of the adjacent CoFe layer. This finally enables control of the magnetization with an electric field via a FE-to-AFM-to-FM domain-pattern transfer across the interface [14,16]. To understand, control, and technologically implement this complex multistage ME transfer chain, we have to be able to track the dynamics of the ME poling. A feasible procedure for this operation consists in recording both the FE domain distribution in BFO and the FM domain pattern induced in the CoFe layer.

A notorious challenge, however, in investigating ferroic heterostructures consists in reaching buried properties and interfacial effects [18], such as in the present case, where the FE state of the BFO film is buried beneath the CoFe layer. One can bypass this by etching away the metallic electrode [14,16], but this inevitably breaks the device functionality and impedes any further investigation of the poling procedure.

In this work, we overcome this limitation by following the ME poling of a BFO/CoFe heterostructure by applying optical second-harmonic generation (SHG) and magnetic force microscopy (MFM) for nondestructive probing.

*deluca@physik.uzh.ch

†Current address: Department of Physics, University of Zurich, Winterthurerstrasse 190, 8057 Zurich, Switzerland

SHG, as described later, is sensitive to the buried FE domain state and MFM is sensitive to the resulting FM order. Tracking the impact of voltage application reveals that the FE order and FM order in BFO and CoFe, respectively, are initially not coupled. Instead, the clamping is activated by the first-time application of an electric field of the order of the BFO coercive field. Following this wake-up effect, we control the evolution of the FM domain distribution in the CoFe layer by adjusting the poling voltage and observe that the main effect of the poling is the generation of differently oriented stripe patterns.

II. EXPERIMENT

Our multilayer is grown by pulsed-laser deposition using a stoichiometric BFO target on a SrRuO₃- (SRO)-buffered (110)-oriented DyScO₃ (DSO) substrate. The film is 50 nm thick and grows with a (001) orientation. Additional growth parameters are described elsewhere [19]. The magnetic CoFe layer and a Pt capping layer, both 3 nm thick, are sputtered *in situ* after the BFO deposition to minimize interface contamination. Finally, by optical lithography and Ar⁺-ion milling, we fabricate a Pt/CoFe bilayer in the shape of a micrometer-sized cross. In Fig. 1, we present the characterization of our device by SHG and MFM. A sketch of the multilayer structure is included as an inset in Fig. 1(a).

With x-ray diffraction, we verify the structural properties of our BFO film. The θ –2 θ scan (not shown) exhibits fringes around the (001) peak, which corroborates the high interfacial quality of the heterostructure. Exploiting the anisotropic in-plane strain exerted by the DSO substrate, we engineer a stripelike FE domain pattern with alternating direction of the stripe polarization in the BFO film [20]. We verify its presence by piezoresponse force microscopy (PFM) in the BFO region not covered by the CoFe/Pt bilayer [see Fig. 1(a)]. When this region is probed, the angular dependence of the [001]_{DSO}-polarized SHG light on the polarization of the incident fundamental light yields four lobes [see Fig. 1(b)]. The deviation from an exact fourfold symmetry of the lobes is caused by the small monoclinic distortion of the BFO unit cell [19,21]. The characteristic SHG polarization dependence associated with our ferroelectric stripe-domain pattern will be useful later when we discuss the domain structure of the BFO layer buried below the CoFe.

We then use MFM to study the FM domain distribution in CoFe [15]. MFM is sensitive to the out-of-plane component of the magnetization and allows tracking of the position of the magnetic domain walls via the stray fields around these walls. The in-plane magnetic state of the CoFe layer grown on top of stripe-domain BFO films is well known from spatially resolved x-ray magnetic circular dichroism, photoemission electron microscopy, and scanning electron microscopy [14–16]. These experiments

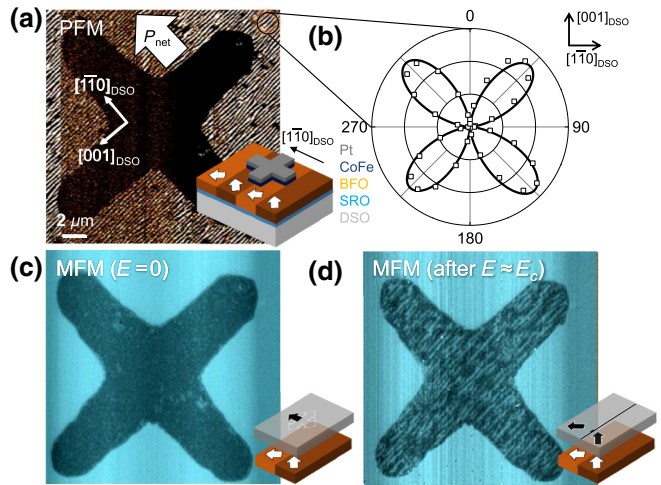


FIG. 1. Magnetoelectric characterization of the Pt/CoFe/BFO/SRO//DSO heterostructure. (a),(b) and (c),(d) refer to the FE and the FM domain patterns, respectively. (a) The in-plane PFM response reveals a FE stripe-domain distribution in BFO, yielding an in-plane net polarization P_{net} (white arrow) along [110]_{DSO}. The cross-shaped metallic electrode prevents the observation of the buried FE BFO domain structure. In the inset, the multilayer structure is depicted. White arrows indicate the in-plane polarization in the single stripes that sums up to P_{net} . (b) SHG polarization analysis on the highlighted circular region of the BFO film in (a). The angular dependence is associated with the rotation of the polarization of the incoming light while the polarization of the outgoing SHG light is fixed parallel to [001]_{DSO} [see Fig. 2(c)]. Open squares and continuous lines represent collected data and the SHG fit, respectively. (c) MFM performed before the first application of a poling voltage reveals uniform distribution of magnetization in CoFe. The inset shows the polarization of BFO (bottom) and magnetization of CoFe (top). Note the absence of their coupling. The CoFe magnetization points in one (black arrow) of the possible (outlined arrows) easy-axis directions. (d) MFM performed after application of an electric poling field close to the BFO coercive field E_c yields magnetic stripes with the same orientation as in the BFO film not covered by CoFe. The description of the inset is as for (c), but now polarization and magnetization are locally coupled.

revealed a magnetization within each CoFe ferromagnetic domain that is collinear with the in-plane projection of the polarization of the corresponding ferroelectric domain in BFO. Since we use the same BFO/CoFe heterostructures as in those earlier experiments, we restrict ourselves in deriving the magnetic domain architecture in our CoFe/Pt bilayer from a MFM stray-field analysis of the domain-wall distribution. Surprisingly, we observe in Fig. 1(c) that in the as-grown heterostructure there is no domain imprint from the BFO film on the overlying CoFe layer. After applying an electric field perpendicular to the sample surface with the scanning-probe-microscope tip, we see in Fig. 1(d) that a stripe pattern similar to the buried BFO domain pattern has appeared in the CoFe. This stripe pattern indicates the presence of an in-plane net magnetization

perpendicular to the stripes and parallel to the net polarization of the BFO stripe pattern beneath [15]. The electric field required to activate the coupling across the interface has to be close to the BFO thin-film coercive field E_c (approximately 600 kV/cm in our device) [19].

The activation of the magnetic coupling (AFM to FM) with an electric field is reminiscent of the wake-up effect observed in ferroelectrics such as Si : HfO, PbZr_xTi_{1-x}O₃, and SrBi₂Ta₂O₉, where a certain number of electric field cycles beyond the coercive field are required to fully activate the switchability of the order parameter [22]. In the present case, the wake-up effect is an important ingredient of the ME coupling dynamics in the BFO/CoFe system. But to track the evolution of this coupling, we need to resolve the exact impact of the external electric field. In particular, we have to find a way to nondestructively monitor how the ME coupling evolves with the applied electric field. For this, we have to quantify the poling of the domain distribution in the buried BFO layer. Conventional characterization techniques such as PFM are not suitable here because they are limited to out-of-plane response in buried ferroelectric layers [Fig. 1(a)] [23]. A nondestructive electron-microscope analysis, as performed in earlier work, is not feasible either because of the changes in the BFO lattice constant occurring as a result of the poling process [24].

To circumvent these limitations, we monitor the evolution of the buried BFO domain pattern under the applied electric field via the angular dependence of the spatially resolved SHG signal and we correlate it with MFM scans of the CoFe domain pattern at the same location. We do this under operating conditions so that we track the ME coupling throughout the poling process.

III. RESULTS

A. Domain-pattern evolution in BFO

SHG is sensitive to the breaking of inversion symmetry in a noncentrosymmetric material and hence is ideal for probing ferroelectric order [19,21,25,26]. The optical frequency doubling is described by $P_i(2\omega) = \epsilon_0 \chi_{ijk} E_j(\omega) E_k(\omega)$, with the rank-3 tensor χ_{ijk} as the SHG susceptibility parametrizing the light-matter interaction [25,26]. The point-group symmetry of the compound determines the allowed χ_{ijk} -tensor components and the relation between them [19,27]. Our domain-engineered BFO film exhibits a stripe-domain state, yielding a net in-plane polarization P_{net} oriented along [110]_{DSO} as shown in Fig. 1(a) [20]. Because the width of the stripe domains (approximately 100 nm) is less than the lateral optical resolution (approximately 1 μm), the nonlinear optical response is directly sensitive to P_{net} rather than to the polarization of the individual domains. SHG therefore distinguishes between regions with differently oriented stripe patterns without resolving individual domains [19].

To observe the evolution of the BFO domain state as a function of increasing bias voltage, we exploit the nondestructive nature of SHG. In our heterostructure, the optical penetration depth is limited by the absorption of light in the metallic electrode. For metallic layers of approximately 10 nm, as in our case, the light is not completely absorbed [19,28]. Hence, we can track the SHG signal generated in the BFO layer buried beneath the CoFe. This signal is readily identified because we did not detect any obscuring magnetization-induced SHG from the CoFe layer [29]. The monoclinic point group m of the BFO films leads to the independent χ_{ijk} -tensor components $\chi_{xxx}, \chi_{xxy}, \chi_{xyy}, \chi_{yyy}, \chi_{yyx}, \chi_{yxz}, \chi_{xzz}, \chi_{yzz}, \chi_{zxx}, \chi_{zzy}$. Some of these components are known to be negligibly small, which allows us to perform a simplified fit of the SHG data with a reduced number of χ_{ijk} fit parameters [19].

Figure 2 shows the SHG response measured at the center of the cross-shaped electrodes for different poling fields. In Figs. 2(a), 2(d), and 2(g) we see the spatially resolved SHG signal of the χ_{xxx} component, while in Figs. 2(b), 2(e), and 2(h) we present the corresponding SHG polarization analysis of the signal measured in the area covered by the electrode. As mentioned, we rotate the polarization of the incoming light while detecting the polarization of the SHG light along [001]_{DSO}. A schematic of the reflection setup is provided in Fig. 2(c). In Figs. 2(f) and 2(i), we sketch the domain pattern derived from the SHG polarization analysis with the model explained in the following. We increase the poling field to determine its influence on the FE domain pattern.

Figures 2(a)–2(c) correspond to the pristine device shown in Fig. 1(a). No voltage has been applied yet, and by MFM we observe the absence of magnetic stripe domains in CoFe as shown in Fig. 1(c). Strikingly, the SHG polarization dependence in the region covered by the electrode [Fig. 2(b)] is the same as in the region not covered by the electrode [Fig. 1(b)] aside from a small decrease in the absolute SHG intensity because of linear absorption of the SHG light passing through the CoFe/Pt layer [19]. We therefore conclude that the FE domain distribution in the buried BFO is the same as in the region not covered by CoFe, with P_{net} along [110]_{DSO} [Fig. 1(a)] [19,20]. This means that the room-temperature sputtering of the metallic layer does not perturb the FE domain state of the underlying BFO film. The FE stripe domains are present as before but we see no evidence of the coupling into the FM layer across the interface.

The response to the poling addressed in Figs. 2(d)–2(i) can essentially have two different outcomes. Limiting our analysis to the in-plane projection of the BFO polarization, we may find [30,31] (i) reversal of the in-plane net polarization of the stripe pattern ($+P_{\text{net}}^{180}$ to $-P_{\text{net}}^{180}$) while keeping the orientation of the stripes as such [32], and (ii) nucleation of an orthogonal set of stripes along with

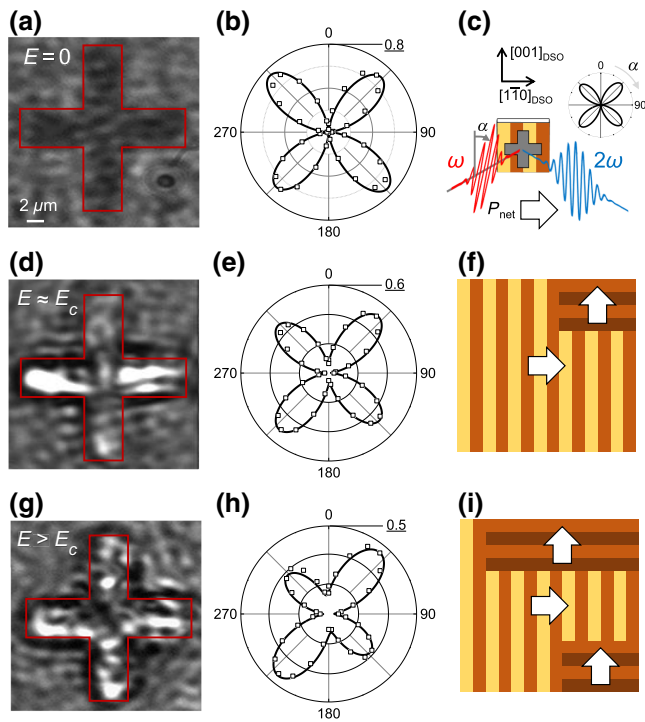


FIG. 2. SHG characterization of the FE BFO layer buried beneath CoFe. (a),(d),(g) Spatially resolved SHG images of light from the χ_{xxx} component collected after application of the indicated electric field. The red contour line highlights the area of the cross-shaped CoFe layer. The lower brightness of this area is caused by linear absorption of the SHG light passing through the CoFe/Pt bilayer. White blotches in (d) and (g) indicate the emergence of additional, inhomogeneously distributed SHG contributions associated with a local rotation of FE net polarization. The exposure time for the SHG images is 1 min. (b),(e),(h) SHG polarization analysis as sketched in (c) after application of the indicated electric field. Open squares and continuous lines represent collected data and the SHG fit, respectively. Underlined numbers are the SHG intensity in arbitrary units. Data points represent the integrated SHG intensity in the center of the CoFe/Pt cross with an exposure time per data point of 10 s. (c) The experimental reflection geometry. (f),(i) Sketch of the multiferroic domain stripe distribution in BFO after the application of an electric field: $E \approx E_c$ and $E > E_c$, respectively. The white arrows indicate the local in-plane net polarization.

a $\pm 90^\circ$ rotation of the in-plane net polarization (P_{net}^{180} to P_{net}^{90}) [19,31].

A partial net polarization reversal (i) changes the overall intensity of the SHG emission due to the destructive interference between SHG contributions from areas with $+P_{\text{net}}^{180}$ and $-P_{\text{net}}^{180}$ [33,34]. It will not lead to new, differently polarized, SHG components. The 90° net polarization rotation (ii), instead, leads to new SHG components, resulting in a change of the angular dependence of the SHG light. As for case (i), destructive interference

between the $+P_{\text{net}}^{90}$ and $-P_{\text{net}}^{90}$ areas will reduce the overall intensity of these new contributions. So, after the poling, four possible stripe-domain patterns with four different orientations of the macroscopic net polarization ($\pm P_{\text{net}}^{180}$, $\pm P_{\text{net}}^{90}$) can in principle coexist below the electrode area [30,31].

Next we investigate the effect of an electric poling field close to the BFO coercive field ($E \approx E_c$). A deviation from the fourfold anisotropy of the SHG polarization dependence in Fig. 2(e) indicates the presence of new SHG components associated with a 90° rotation of the net polarization. This is also visible in the spatially resolved SHG image in Fig. 2(d), where white blotches indicate the position of reoriented ferroelectric domains with $\pm P_{\text{net}}^{90}$ since these lead to new SHG components. Although the polarization-anisotropy change is small compared with that in the as-grown device [see Figs. 2(e) and 2(b), respectively], the quantitative analysis below shows that the SHG measurement is very sensitive to the presence of new χ_{ijk} components [19,25]. Application of a larger poling voltage [see Fig. 2(g)] results in a stronger deviation from the original polarization anisotropy [Fig. 2(h)], revealing an increase of the area yielding a 90° rotation of P_{net} .

To quantify the amount of stripe domains reoriented by the poling voltage, we fit the polarization dependence of the SHG signal in Figs. 2(b), 2(e), and 2(h) using the SHG susceptibilities derived from Fig. 1(b) [19] and we introduce $\delta P_{\text{net}}^{\pm 180}$ and $\delta P_{\text{net}}^{\pm 90}$ as fit parameters representing the areal fractions in the sample covered by the four possible types of stripe-domain patterns introduced above [25,30]. Only three of these are independent because $\sum \delta P_{\text{net}}^{\pm(90,180)} = 1$ [25,35]. The fit values are reported in Table I. We also explicitly report the percentage of areas with stripes oriented orthogonal ($\delta P_{\text{net}}^{90} = \delta P_{\text{net}}^{+90} + \delta P_{\text{net}}^{-90}$) to the as-grown state because these are identified by the different orientation of the domain stripes in the MFM scans discussed in the next section. There is only a minor mixture of domains of $+P_{\text{net}}^{180}$ and $-P_{\text{net}}^{180}$. This is expected as it was established that an out-of-plane voltage will result in a full reversal of the in-plane polarization in Pt/CoFe/BFO/SRO capacitors [14,16,24]. The 90° rotation of the polarization leads to a dominance of one direction ($+P_{\text{net}}^{90}$) over the other ($-P_{\text{net}}^{90}$) [see Fig. 2(f)]. Hence, from the SHG analysis, we derive that before the voltage application, the domain distribution in the BFO corresponds to the as-grown state, with a net in-plane polarization $+P_{\text{net}}^{180}$ pointing along $[1\bar{1}0]_{\text{DSO}}$ [14,19,20]. With an electric field intensity of $E \approx E_c$, we find $\delta P_{\text{net}}^{90} \approx 16\%$ for the stripe domains with a $\pm 90^\circ$ rotation of P_{net} . By increasing the poling voltage, we are nucleating a larger amount of stripe domains that are polarized along $[001]_{\text{DSO}}$, orthogonal to the as-grown direction ($\delta P_{\text{net}}^{90} \approx 40\%$) [see Fig. 2(i)].

TABLE I. Quantification of the magnetoelectric poling. Areal fractions of the possible orientations of P_{net} and M_{net} in the BFO/CoFe system are shown for different applied electric fields. The values are derived from fits of the SHG polarization dependence in Fig. 2 (see the text) and application of a k -means clustering algorithm to the MFM scans in Fig. 3. E is the electric poling field, $\delta P_{\text{net}}^{+180}$, $\delta P_{\text{net}}^{-180}$, $\delta P_{\text{net}}^{+90}$, and $\delta P_{\text{net}}^{-90}$ are the areal fractions of the four types of FE stripe-domain patterns (see the text), $\delta P_{\text{net}}^{90} = \delta P_{\text{net}}^{+90} + \delta P_{\text{net}}^{-90}$ is the areal fraction of FE domain stripes in BFO oriented along $[1\bar{1}0]_{\text{DSO}}$, and $\delta M_{\text{net}}^{90}$ is the areal fraction of FM domain stripes in CoFe oriented along $[1\bar{1}0]_{\text{DSO}}$. Values are given as a percentage.

Electric field	SHG					$\delta M_{\text{net}}^{90}$
	$\delta P_{\text{net}}^{+180}$	$\delta P_{\text{net}}^{-180}$	$\delta P_{\text{net}}^{+90}$	$\delta P_{\text{net}}^{-90}$	$\delta P_{\text{net}}^{90}$	
$E = 0$	98 ± 1	0 ± 1	2 ± 1	0 ± 1	2 ± 2	No coupling
$E \approx E_c$	5 ± 1	79 ± 1	16 ± 1	0 ± 1	16 ± 2	12 ± 5
$E > E_c$	4 ± 1	56 ± 1	39 ± 1	1 ± 1	40 ± 2	27 ± 3

B. Magnetic domain distribution in CoFe

We use now MFM to visualize the effect that the response of the ferroelectric BFO stripe domains to the poling voltage has on the magnetic domain distribution of the overlying CoFe layer. A weak in-plane magnetic field applied during the MFM scans allows us to readily distinguish areas with 180° and 90° stripe-domain patterns, as we explain in the following.

When CoFe is magnetically coupled to BFO, it shows a magnetic easy axis perpendicular to the direction of the domain stripes. Since the stripes run along the $[001]_{\text{DSO}}$ direction, the easy axis points along the $[1\bar{1}0]_{\text{DSO}}$ direction. Hence, the coercive magnetic field $H_{\parallel}||P_{\text{net}}$ needed to uniformly align the CoFe magnetization is lower than the coercive field $H_{\perp}\perp P_{\text{net}}$ [15]. By application of a field $H_{\parallel} < H < H_{\perp}$, only stripes parallel to the H direction will remain. By applying H along $[1\bar{1}0]_{\text{DSO}}$ or $[001]_{\text{DSO}}$, we can thus distinguish the regions with stripes along $[1\bar{1}0]_{\text{DSO}}$ or $[001]_{\text{DSO}}$, respectively. We find $\mu_0 H_{\parallel} < 10$ mT [36] and $\mu_0 H_{\perp} > 110$ mT, and therefore choose $\mu_0 H = 50$ mT. In Fig. 3 we present the resulting MFM images for increasing electric poling field in each case for H applied along $[1\bar{1}0]_{\text{DSO}}$ or $[001]_{\text{DSO}}$, respectively.

First, we discuss the case of the as-grown device. As seen from Fig. 1(c), no magnetic stripe domains are observed. The CoFe yields uniform magnetization for H applied along both $[001]_{\text{DSO}}$ and $[1\bar{1}0]_{\text{DSO}}$ [Figs. 3(a) and 3(b)]. The contrast at the edges of the cross-shaped electrode confirms that the layer is uniformly in-plane magnetized, always parallel to the direction of H . Hence, the pristine CoFe film behaves magnetically isotropically with respect to the DSO in-plane crystallographic directions, corroborating that before the application of an electric field there is no ME coupling between the BFO and the CoFe layer as sketched in Fig. 3(c).

The situation changes after application of an electric field $E \approx E_c$. MFM now reveals magnetic stripes with an orientation as in the underlying BFO layer [see Fig. 3(d) and also Fig. 1(d)]. When the in-plane magnetic field is pointing along $[001]_{\text{DSO}}$ [Fig. 3(d)], we obtain a dense pattern of stripes along $[001]_{\text{DSO}}$ all across the area covered

by the electrode. In contrast, with a magnetic field along the $[1\bar{1}0]_{\text{DSO}}$ direction [Fig. 3(e)], we obtain an almost-uniform magnetization, yet with a few orthogonal stripes. Thus, the distribution of domain stripes in the ferromagnetic CoFe film matches that in the ferroelectric BFO film: the ME transfer of the net polarization to the net magnetization is now active [14–16,24] [Fig. 3(f)]. The activation of this transfer requires an electric field close to the BFO coercive field, indicated by the beginning 90° rotation of the BFO stripe domains. After application of a larger bias voltage, the magnetic stripes become more equally distributed between the $[001]_{\text{DSO}}$ direction and the $[1\bar{1}0]_{\text{DSO}}$ direction [Figs. 3(g) and 3(h)]. The higher field promotes the 90° rotation of the BFO stripe domains, coupled to the 90° rotation of the CoFe stripe domains.

We quantify the areal distribution of the magnetic stripes using a k -means clustering algorithm [37], with the results listed in the $\delta M_{\text{net}}^{90}$ column in Table I. We obtain $\delta M_{\text{net}}^{90} \approx 12\%$ for $E \approx E_c$ and $\delta M_{\text{net}}^{90} \approx 27\%$ for $E > E_c$. This is in reasonable agreement with the SHG data ($\delta P_{\text{net}}^{90}$). The difference that we observe is most likely related to the incoherent (i.e., noninterfering) contributions to the SHG signal that are caused by the limited spatial coherence of our laser beam. These are not included in the fit of $\delta P_{\text{net}}^{\pm(90,180)}$, an approximation introducing a small systematic error into the SHG fits [25].

IV. SUMMARY

In summary, using optical SHG and MFM as nondestructive *in operando* probes, we track the response of the ME coupling in a BFO/CoFe heterostructure to applied electric fields. With the SHG analysis we precisely quantify the FE domain distribution of BFO buried below the metallic electrode as a function of increasing bias voltage. MFM provides the complementary FM domain structure in CoFe. Strikingly, we find that the interfacial coupling between the FE BFO and the FM CoFe needs to be activated by an initial applied electric field on the order of the coercive field. Clarification of the origin of this wake-up effect will require detailed studies on strain, magnetic

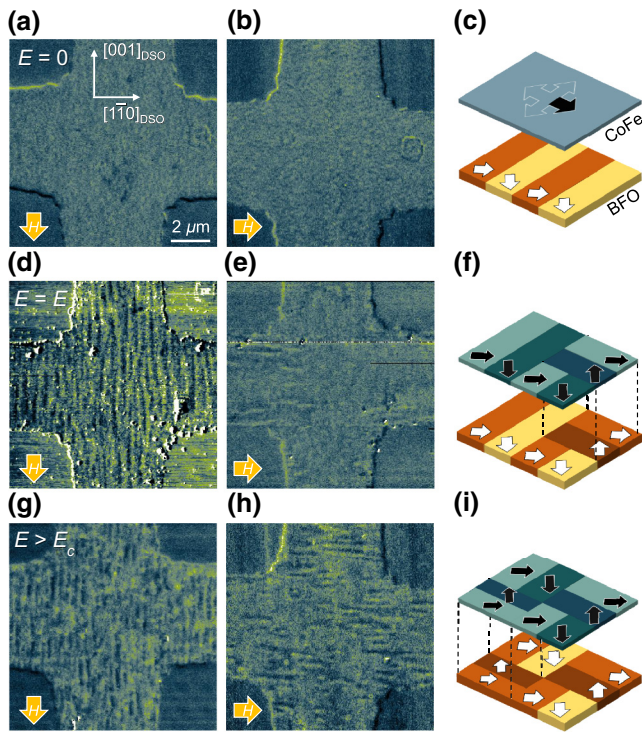


FIG. 3. MFM characterization of the cross-shaped FM CoFe layer. The spatially resolved MFM scans show the magnetic domain structure of CoFe after the application of the indicated electric field. MFM scans are recorded in the presence of an in-plane magnetic field of $\mu_0 H = 50$ mT along $[001]_{\text{DSO}}$ (a),(d),(g) or $[1\bar{1}0]_{\text{DSO}}$ (b),(e),(h); see yellow arrows. (c),(f),(i) The ME BFO/CoFe domain-pattern transfer derived from the MFM scans. White arrows indicate the local BFO in-plane polarization, while the black arrows indicate the CoFe magnetization. (a),(b) The pristine CoFe film yields a uniform in-plane magnetization. The lack of magnetic anisotropy indicates the suppression of the ME BFO/CoFe coupling. (d),(e) After application of an electric field $E \approx E_c$. The magnetic field oriented along $[001]_{\text{DSO}}$ (d) or $[1\bar{1}0]_{\text{DSO}}$ (e) filters out areas with magnetic stripe domains along $[1\bar{1}0]_{\text{DSO}}$ or $[001]_{\text{DSO}}$, respectively (see the text). Stripes are mainly oriented along $[001]_{\text{DSO}}$, parallel to the as-grown buried FE domains. (g),(h) Same as (d),(e) after application of an electric field $E > E_c$. The fraction of magnetic stripes oriented along $[1\bar{1}0]_{\text{DSO}}$ has increased.

anisotropy, interface chemistry, and higher-order magnetoelectric coupling effects. Once the BFO coercive field is exceeded, we observe nucleation of an orthogonal set of stripes with a $\pm 90^\circ$ rotation of the in-plane net polarization. The areal fraction of these orthogonal stripes scales with the applied electric poling voltage.

Thus, our *in operando* access to ME switching, enabled by noninvasive probing of the FE and FM order, provides access to the ME BFO/CoFe coupling processes with an unprecedented degree of detail. The *in operando* access to the ME coupling is also the first step toward the observation of room-temperature reversible switching dynamics

down to the ultrafast timescale, an important prerequisite for device applications.

ACKNOWLEDGMENTS

The authors thank Ramamoorthy Ramesh, University of California, Berkeley, for valuable discussion. This research was supported by the EU European Research Council (Advanced Grant No. 694955—INSEETO) and the Swiss National Science Foundation (Grant No. 200020-172775).

All authors discussed the results and contributed to the completion of the manuscript. G.D.L. performed the SHG measurements and developed the SHG fitting model. M.T. performed the multiferroic heterostructure growth. J.M. performed the optical lithography and ion milling. M.T., P.S., and G.D.L. performed the PFM and MFM analysis under electric and magnetic fields. D.M., M.F., and M.T. designed the experiment and supervised the work.

- [1] J. F. Scott, Data storage: Multiferroic memories, *Nat. Mater.* **6**, 256 (2007).
- [2] M. Bibes and A. Barthélémy, Multiferroics: Towards a magnetoelectric memory, *Nat. Mater.* **7**, 425 (2008).
- [3] M. Bibes, J. E. Villegas, and A. Barthélémy, Ultrathin oxide films and interfaces for electronics and spintronics, *Adv. Phys.* **60**, 5 (2011).
- [4] M. Trassin, Low energy consumption spintronics using multiferroic heterostructures, *J. Phys.: Condens. Matter* **28**, 033001 (2016).
- [5] M. Fiebig, T. Lottermoser, D. Meier, and M. Trassin, The evolution of multiferroics, *Nat. Rev. Mater.* **1**, 16046 (2016).
- [6] C.-W. Nan, M. I. Bichurin, S. Dong, D. Viehland, and G. Srinivasan, Multiferroic magnetoelectric composites: Historical perspective, status, and future directions, *J. Appl. Phys.* **103**, 031101 (2008).
- [7] C. A. F. Vaz, Electric field control of magnetism in multiferroic heterostructures, *J. Phys.: Condens. Matter* **24**, 333201 (2012).
- [8] F. Matsukura, Y. Tokura, and H. Ohno, Control of magnetism by electric fields, *Nat. Nanotechnol.* **10**, 209 (2015).
- [9] J.-M. Hu, L.-Q. Chen, and C.-W. Nan, Multiferroic heterostructures integrating ferroelectric and magnetic materials, *Adv. Mater.* **28**, 15 (2016).
- [10] C. Thiele, K. Dörr, O. Bilani, J. Rödel, and L. Schultz, Influence of strain on the magnetization and magnetoelectric effect in $\text{La}_{0.7}\text{A}_{0.3}\text{MnO}_3/\text{PMN-PT}(001)$ ($\text{A} = \text{Sr}, \text{Ca}$), *Phys. Rev. B* **75**, 054408 (2007).
- [11] D. Chiba, M. Sawicki, Y. Nishitani, Y. Nakatani, F. Matsukura, and H. Ohno, Magnetization vector manipulation by electric fields, *Nature* **455**, 515 (2008).
- [12] T. Maruyama, Y. Shiota, T. Nozaki, K. Ohta, N. Toda, M. Mizuguchi, A. A. Tulapurkar, T. Shinjo, M. Shiraishi, S. Mizukami, Y. Ando, and Y. Suzuki, Large voltage-induced magnetic anisotropy change in a few atomic layers of iron, *Nat. Nanotechnol.* **4**, 158 (2009).

- [13] J. A. Mundy, C. M. Brooks, M. E. Holtz, J. A. Moyer, H. Das, A. F. Rébola, J. T. Heron, J. D. Clarkson, S. M. Disseler, Z. Liu, A. Farhan, R. Held, R. Hovden, E. Padgett, Q. Mao, H. Paik, R. Misra, L. F. Kourkoutis, E. Arenholz, A. Scholl, J. A. Borchers, W. D. Ratcliff, R. Ramesh, C. J. Fennie, P. Schiffer, D. A. Muller, and D. G. Schlom, Atomically engineered ferroic layers yield a room-temperature magnetoelectric multiferroic, *Nature* **537**, 523 (2016).
- [14] J. T. Heron, M. Trassin, K. Ashraf, M. Gajek, Q. He, S. Y. Yang, D. E. Nikonov, Y.-H. Chu, S. Salahuddin, and R. Ramesh, Electric-Field-Induced Magnetization Reversal in a Ferromagnet-Multiferroic Heterostructure, *Phys. Rev. Lett.* **107**, 217202 (2011).
- [15] M. Trassin, J. D. Clarkson, S. R. Bowden, J. Liu, J. T. Heron, R. J. Paull, E. Arenholz, D. T. Pierce, and J. Unguris, Interfacial coupling in multiferroic/ferromagnet heterostructures, *Phys. Rev. B* **87**, 134426 (2013).
- [16] J. T. Heron, J. L. Bosse, Q. He, Y. Gao, M. Trassin, L. Ye, J. D. Clarkson, C. Wang, J. Liu, S. Salahuddin, D. C. Ralph, D. G. Schlom, J. Iñiguez, B. D. Huey, and R. Ramesh, Deterministic switching of ferromagnetism at room temperature using an electric field, *Nature* **516**, 370 (2014).
- [17] T. Zhao, A. Scholl, F. Zavaliche, K. Lee, M. Barry, A. Doran, M. P. Cruz, Y. H. Chu, C. Ederer, N. A. Spaldin, R. R. Das, D. M. Kim, S. H. Baek, C. B. Eom, and R. Ramesh, Electrical control of antiferromagnetic domains in multiferroic BiFeO₃ films at room temperature, *Nat. Mater.* **5**, 823 (2006).
- [18] G. De Luca, M. D. Rossell, J. Schaab, N. Viart, M. Fiebig, and M. Trassin, Domain wall architecture in tetragonal ferroelectric thin films, *Adv. Mater.* **29**, 1605145 (2017).
- [19] M. Trassin, G. De Luca, S. Manz, and M. Fiebig, Probing ferroelectric domain engineering in BiFeO₃ thin films by second harmonic generation, *Adv. Mater.* **27**, 4871 (2015).
- [20] Y.-H. Chu, Q. He, C.-H. Yang, P. Yu, L. W. Martin, P. Shafer, and R. Ramesh, Nanoscale control of domain architectures in BiFeO₃ thin films, *Nano Lett.* **9**, 1726 (2009).
- [21] A. Kumar, S. Denev, R. J. Zeches, E. Vlahos, N. J. Podraza, A. Melville, D. G. Schlom, R. Ramesh, and V. Gopalan, Probing mixed tetragonal/rhombohedral-like monoclinic phases in strained bismuth ferrite films by optical second harmonic generation, *Appl. Phys. Lett.* **97**, 112903 (2010).
- [22] D. Zhou, J. Xu, Q. Li, Y. Guan, F. Cao, X. Dong, J. Müller, T. Schenk, and U. Schröder, Wake-up effects in Si-doped hafnium oxide ferroelectric thin films, *Appl. Phys. Lett.* **103**, 192904 (2013).
- [23] S. V. Kalinin, B. J. Rodriguez, S.-H. Kim, S.-K. Hong, A. Gruverman, and E. A. Eliseev, Imaging mechanism of piezoresponse force microscopy in capacitor structures, *Appl. Phys. Lett.* **92**, 152906 (2008).
- [24] J. Unguris, S. R. Bowden, D. T. Pierce, M. Trassin, R. Ramesh, S.-W. Cheong, S. Fackler, and I. Takeuchi, Simultaneous imaging of the ferromagnetic and ferroelectric structure in multiferroic heterostructures, *APL Mater.* **2**, 076109 (2014).
- [25] S. A. Denev, T. T. A. Lummen, E. Barnes, A. Kumar, and V. Gopalan, Probing ferroelectrics using optical second harmonic generation, *J. Am. Ceram. Soc.* **94**, 2699 (2011).
- [26] J. Nordlander, G. De Luca, N. Strkalj, M. Fiebig, and M. Trassin, Probing ferroic states in oxide thin films using optical second harmonic generation, *Appl. Sci.* **8**, 570 (2018).
- [27] D. Fröhlich, T. Kiefer, S. Leute, and T. Lottermoser, Non-linear spectroscopy of antiferromagnetics, *Appl. Phys. B: Lasers Opt.* **68**, 465 (1999).
- [28] Z. Q. Qiu and S. D. Bader, Surface magneto-optic Kerr effect (SMOKE), *J. Magn. Magn. Mater.* **200**, 664 (1999).
- [29] A. Kirilyuk and T. Rasing, Magnetization-induced-second-harmonic generation from surfaces and interfaces, *J. Opt. Soc. Am. B* **22**, 148 (2005).
- [30] S. K. Streiffer, C. B. Parker, A. E. Romanov, M. J. Lefevre, L. Zhao, J. S. Speck, W. Pompe, C. M. Foster, and G. R. Bai, Domain patterns in epitaxial rhombohedral ferroelectric films. I. Geometry and experiments, *J. Appl. Phys.* **83**, 2742 (1998).
- [31] N. Balke, S. Choudhury, S. Jesse, M. Huijben, Y. H. Chu, A. P. Baddorf, L. Q. Chen, R. Ramesh, and S. V. Kalinin, Deterministic control of ferroelastic switching in multiferroic materials, *Nat. Nanotechnol.* **4**, 868 (2009).
- [32] S. H. Baek, H. W. Jang, C. M. Folkman, Y. L. Li, B. Winchester, J. X. Zhang, Q. He, Y. H. Chu, C. T. Nelson, M. S. Rzchowski, X. Q. Pan, R. Ramesh, L. Q. Chen, and C. B. Eom, Ferroelastic switching for nanoscale non-volatile magnetoelectric devices, *Nat. Mater.* **9**, 309 (2010).
- [33] J. Kaneshiro, Y. Uesu, and T. Fukui, Visibility of inverted domain structures using the second harmonic generation microscope: Comparison of interference and non-interference cases, *J. Opt. Soc. Am. B* **27**, 888 (2010).
- [34] G. De Luca, N. Strkalj, S. Manz, C. Bouillet, M. Fiebig, and M. Trassin, Nanoscale design of polarization in ultra-thin ferroelectric heterostructures, *Nat. Commun.* **8**, 1419 (2017).
- [35] Y. Barad, J. Lettieri, C. D. Theis, D. G. Schlom, V. Gopalan, J. C. Jiang, and X. Q. Pan, Probing domain microstructure in ferroelectric Bi₄Ti₃O₁₂ thin films by optical second harmonic generation, *J. Appl. Phys.* **89**, 1387 (2001).
- [36] L. You, B. Wang, X. Zou, Z. S. Lim, Y. Zhou, H. Ding, L. Chen, and J. Wang, Origin of the uniaxial magnetic anisotropy in La_{0.7}Sr_{0.3}MnO₃ on stripe-domain BiFeO₃, *Phys. Rev. B* **88**, 184426 (2013).
- [37] J. A. Hartigan and M. A. Wong, Algorithm AS 136: A k-means clustering algorithm, *Appl. Stat.* **28**, 100 (1979).